Model-free detection of physical order from scattering and imaging data using escort-weighted Shannon entropy and divergence matrices

Jared Coles [1,2] Arthur R. C. McCray [1,3] Yue Li [1] Bryan T. Fichera [1] Yan Wu [4] Yiqing Hao [4] Daniel Phelan [1] Yue Cao [1] Raymond Osborn [1] Charudatta Phatak [1,5] Stephan Rosenkranz [1] and Yu Li [1,*]

[1] Materials Science Division, Argonne National Laboratory, Lemont, Illinois 60439, USA
[2] Department of Physics, Northern Illinois University, DeKalb, Illinois 60115, USA
[3] Department of Materials Science and Engineering, Stanford University, Stanford, California, USA
[4] Neutron Scattering Division, Oak Ridge National Laboratory, Oak Ridge, Tennessee 37831, USA
[5] Department of Materials Science and Engineering, Northwestern University, Evanston, Illinois 60208, USA

(Received 28 January 2026; accepted 27 July 2026; published 27 August 2026)

We demonstrate a model-free data analysis framework that leverages escort-weighted Shannon entropy and several divergence matrices to detect phase transitions in scattering and imaging datasets. By establishing a connection between physical entropy and informational entropy, this approach provides a sensitive method for identifying phase transitions without a physical model or order parameter. We further show that pairwise divergence matrices, in particular, Kullback-Leibler divergence, Jeffrey divergence, Jensen-Shannon divergence, and difference Kullback-Leibler divergence, provide more comprehensive measures of statistical changes than scalar entropy alone. Our approach successfully detects the onset of both long- and short-range order in neutron and x-ray scattering data, as well as a nontrivial phase transition in magnetic skyrmion lattices observed through Lorentz-transition electron microscopy. These results establish a framework for fast, automated, model-free detection of physical order in experimental data with broad applications in materials science and condensed matter physics.

DOI: 10.1103/5txt-skp5

I. INTRODUCTION

Entropy stands as one of the most fundamental concepts in physics. It is intimately linked to the second law of thermodynamics and is central to our understanding of diverse phenomena, from frustrated magnetism [1,2] and black hole radiation [3] to emergent gravity [4] and information theory [5,6]. In thermodynamics, entropy provides a measure of disorder and is generally defined via the Gibbs formulation, $S_{\text{Gibbs}} = -k_B \sum p_i \ln(p_i)$, where p_i is the probability of occupying a microstate i and k_B is the Boltzmann constant. Likewise in information theory, the Shannon entropy that possesses a similar mathematical form (defined in the next section) quantifies the average amount of information or uncertainty in a dataset. While thermodynamic entropy is often regarded as a physical quantity, Shannon entropy is typically viewed as "subjective," measuring the incompleteness of an observer's knowledge of a system's state. E. T. Jaynes, in one of his seminal works, proposed a fundamental conceptual connection between the two formulations of entropy [7,8], where the thermodynamic entropy is derived from Shannon entropy through principles of statistical inference. This connection was further developed by Landauer [9] and experimentally validated in several studies [10,11], which showed that erasing information necessarily leads to the dissipation of heat, revealing an intrinsic entropy cost to information processing. It is now well established that there exists an entire family of entropy measures, and some of them, such as quantum Fisher information [12], have attracted renewed interest for their usefulness in quantifying entanglement and other physical phenomena across a range of scientific disciplines.

Here, we focus on scattering and imaging experiments, where the image and volumetric data encode information about the physical state of a material. Traditional data analysis often focuses on identifying peaks in scattering spectra (e.g., as a function of energy or momentum transfer). In condensed matter physics, the intensities of peaks at ordering wave vectors can be used to track order parameters as functions of thermodynamic control parameters, such as temperature, pressure, and applied magnetic or electric fields [13–15]. However, this approach is only useful if the ordering wave vector can be identified; there are risks of oversight or selection bias if ordering occurs at unknown wave vectors that are unrecognized by experimenters or data analysis routines. This risk has been reduced by the introduction of large-area detectors, which dramatically expand reciprocal-space coverage [16] and enable rapid collection of large datasets with many potential regions of interest. Nevertheless, the resulting increase in data volume creates significant challenges for rapid analysis, as conventional model-driven methods can be time-consuming and often require sophisticated techniques [17,18].

To address these challenges, we assume a hypothetical mapping between the physical state distribution and the

*Contact author: yu.li@anl.gov

Published by the American Physical Society under the terms of the Creative Commons Attribution 4.0 International license. Further distribution of this work must maintain attribution to the author(s) and the published article's title, journal citation, and DOI.

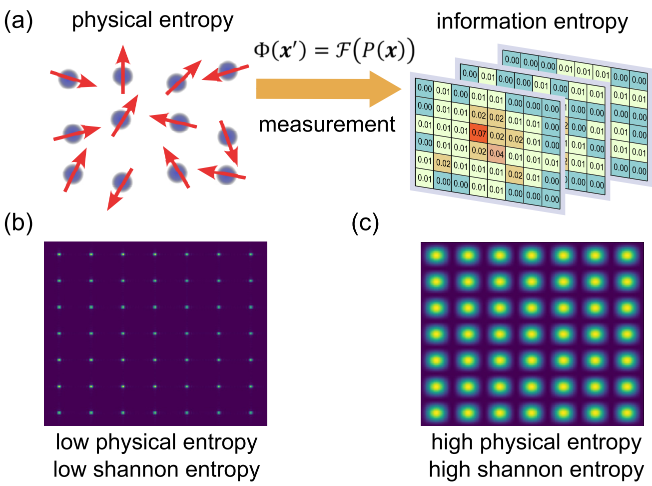

FIG. 1. (a) Schematic illustration of the relationship between physical entropy and information entropy. (b) Diffraction intensity from perfectly ordered materials where low physical entropy corresponds to low Shannon entropy. (c) Diffraction intensity from disordered materials, where high physical entropy is reflected by Shannon entropy in the data.

distribution of intensities in measurement (data) space:

$$\Phi(x_1', x_2', \ldots) = \mathcal{F}(P(x_1, x_2, \ldots)), \tag{1}$$

where $\Phi(x_1', x_2', \ldots)$ denotes a probability distribution in a high-dimensional data space with coordinates $x_1', x_2', \ldots,$ and $P(x_1, x_2, \ldots)$ is the probability distribution over the system's phase space with physical degrees of freedom x_1, $x_2, \ldots$. By connecting the thermodynamic entropy of the sample to the informational entropy of the measured datasets (Fig. 1) through this mapping, we develop an information-theory-inspired analysis framework that operates directly on measured data without requiring an explicit physical model. Based on the escort distribution and relative entropy (divergence), we demonstrate that this framework captures the onset of long- and short-range magnetic and structural order, as well as a nontrivial two-dimensional (2D) phase transition in magnetic skyrmion lattices. We present case studies spanning a range of data types, including neutron diffraction data on $Eu_3Sn_2S_7$, x-ray scattering on $Cd_2Re_2O_7$ [18], and Lorentz-transition electron microscopy (L-TEM) images of magnetic skyrmions in Fe_3GeTe_2 [19]. We show that escort-weighted entropy and pairwise divergence matrices serve as effective and model-free indicators of potential phase changes and transitions. We emphasize that this development is not intended to replace conventional physics-based analysis but rather provides a complementary method to rapidly identify candidate phase transitions on raw measured data. Our framework can be integrated into existing analysis pipelines and used as input for advanced machine-learning (ML) workflows [17]. These results highlight opportunities to leverage informational and statistical tools for automated, model-free analysis of large scientific datasets.

II. THEORETICAL AND METHODOLOGICAL FRAMEWORK

A. Escort distribution and artificial temperature

In general, scattering or imaging datasets in one- or multidimensional spaces can be normalized into a probability distribution $P = \{p_i\}$, where p_i represents the normalized intensity at pixel or voxel i and satisfies the normalization condition $\sum_i p_i = 1$. Such datasets can be represented in various formats, such as detector pixels, wave vectors in $\boldsymbol{Q}$ space, positional indices in real space, or even time steps along a temporal axis. The Shannon entropy, quantifying the information content of a distribution, is defined by

$$H(p) = -\sum_i p_i \log_2 p_i. \tag{2}$$

In a typical diffraction experiment on a perfectly ordered crystal, the diffraction intensity distribution exhibits Bragg peaks that are ideally δ functions, with zero intensity elsewhere. The low thermodynamic entropy of a crystal with infinite long-range order is reflected in the minimal Shannon entropy of the corresponding diffraction dataset [Fig. 1(b)]. In contrast, if the atoms are completely random, with neither long- nor short-range order, the scattering pattern approaches a uniform distribution, and the information entropy is maximized.

While this connection is intuitive and not mandated by fundamental principles, it is reasonable to postulate that the transformation functional

$$\Phi(\boldsymbol{x}') = \mathcal{F}(P(\boldsymbol{x})) \tag{3}$$

is monotonic in the sense that it preserves the ordering of state probabilities. Specifically, if the physical distribution satisfies

$$p_1 \leqslant p_i \leqslant \cdots \leqslant p_j \leqslant \cdots \leqslant p_N,$$

where N is the total number of states (irrespective of symmetry or periodicity), then the transformed distribution preserves this ordering:

$$q_1 \leqslant q_i \leqslant \cdots \leqslant q_j \leqslant \cdots \leqslant q_N.$$

To formalize this idea, we adopt the escort distribution transformation [20,21], defined by

$$q_i = \frac{p_i^n}{\sum_{k=1}^{N} p_k^n}, \tag{4}$$

where p_i represents the probability associated with pixel/voxel i in $P(\boldsymbol{x})$, q_i is the corresponding probability in $\Phi(\boldsymbol{x}')$, and $n = \frac{1}{T_a}$. Here, T_a acts as an effective "artificial temperature" that controls the relative weight of each state (pixel or voxel). Apparently, this mapping is monotonic for $n > 0$, and the original distribution is recovered when $n = 1$ (equivalently, $T_a = 1$).

B. Relative entropy and divergence matrices

While Shannon entropy characterizes the overall content of information in a dataset, changes across a phase transition as a function of external parameters can be subtle. For instance, in a neutron diffraction study of temperature-dependent magnetic order, the Shannon entropy might be dominated by the nearly constant intensity of structural Bragg peaks across the transition. To increase sensitivity to such changes, we introduce relative entropy, mirroring the Kullback-Leibler divergence (KLD) [22] in information theory:

$$D_{\mathrm{KL}}(P \parallel Q) = \sum_i p_i \log\left(\frac{p_i}{q_i}\right). \quad (5)$$

Here, $D_{\mathrm{KL}}(P \parallel Q)$ denotes the divergence between two probability distributions $P = \{p_i\}$ and $Q = \{q_i\}$ measured under two different conditions (e.g., temperatures or fields); in our divergence matrix, it corresponds to the matrix element comparing those two conditions. In general, KLD quantifies how much information is lost when P is approximated by Q and is inherently asymmetric: $D_{\mathrm{KL}}(P \parallel Q) \neq D_{\mathrm{KL}}(Q \parallel P)$. In practice, symmetric variants are more commonly used, including the Jeffrey divergence (JD) [23]:

$$D_{\mathrm{J}}(P \parallel Q) = \tfrac{1}{2}D_{\mathrm{KL}}(P \parallel Q) + \tfrac{1}{2}D_{\mathrm{KL}}(Q \parallel P), \quad (6)$$

and the Jensen-Shannon divergence (JSD) [24]:

$$D_{\mathrm{JS}}(P \parallel Q) = \tfrac{1}{2}D_{\mathrm{KL}}(P \parallel M) + \tfrac{1}{2}D_{\mathrm{KL}}(Q \parallel M), \quad (7)$$

where $M = \frac{1}{2}(P + Q)$. A key advantage of JSD is that it is bounded: $0 \leqslant D_{\mathrm{JS}}(P \parallel Q) \leqslant \log 2$, making it widely used in bioinformatics, social sciences, and deep learning [25,26]. In addition to these symmetric forms, we introduce the difference KLD (d-KLD or Δ-KLD):

$$D_{\text{d-KL}}(P \parallel Q) = D_{\mathrm{KL}}(P \parallel Q) - D_{\mathrm{KL}}(Q \parallel P), \quad (8)$$

which measures directional changes of entropy between two datasets. We note that these directional differences should not be directly interpreted as thermodynamic irreversibility and leave further discussion of their physical interpretation to future work.

When arranged into pairwise matrices over a sequential series of measurements, all four divergence measures exhibit blocklike structures whose boundaries separate statistically similar datasets from dissimilar ones, serving as visual indicators of phase transitions. However, there are important differences. The KLD matrix has nonidentical upper and lower triangles due to its asymmetry. The JD and JSD preserve symmetry by either averaging the two KLD directions, or by comparing each distribution to their mixture M, with the additional advantage of being bounded in [0, ln 2]. The Δ-KLD is unique because it can take both positive and negative values. This property is particularly advantageous for pseudocolor visualization, since the zero crossing provides a natural and robust boundary separating regions of the matrix, as demonstrated below. However, as discussed below, we find that different measures are more sensitive to different types of transitions, e.g., long-range versus short-range transitions, and therefore recommend examining all four matrices in practice for determination of changes in physical order or character of fluctuations.

III. EXPERIMENTAL METHODS

We selected three full sets of representative temperature/field-dependent data from neutron scattering, x-ray scattering, and L-TEM images, respectively. Neutron diffraction

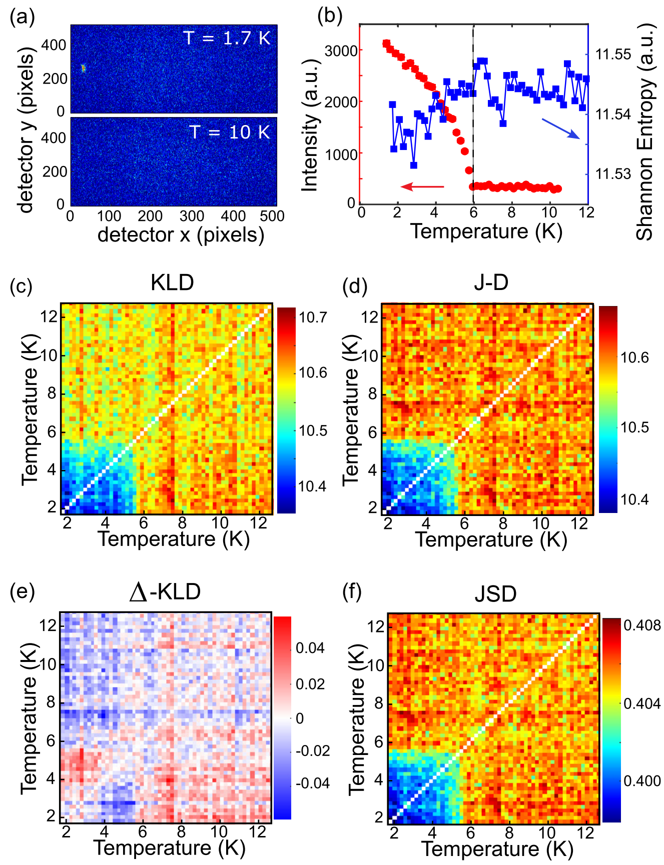

FIG. 2. (a) Detector image of the magnetic Bragg peak in $Eu_3Sn_2S_7$ at $q = (-0.5, 1.5, 0)$. (b) Temperature dependence of the peak intensity (red) and the Shannon entropy (blue). (c)–(f), KLD, JD, Δ-KLD, and JSD matrices computed from the detector images at a series of temperatures. Blocks with similar colors in the divergence matrices indicate statistically similar states, and their boundaries correspond to the phase transition at 6 K.

data on a single crystal of $Eu_3Sn_2S_7$ were collected on the HB-3A (DEMAND) beamline at Oak Ridge National Laboratory. Both temperature and magnetic field dependences were measured. Using a two-dimensional area detector, typical low-temperature data contain a single magnetic Bragg peak at wave vector $Q = (-0.5, 1.5, 0)$ r.l.u. (reciprocal lattice units) and surrounding background, as shown in Fig. 2(a). This material exhibits an interesting magnetic Cairo lattice [27,28] and undergoes two magnetic transitions at 6 and 4 K at zero field, plus a series of metamagnetic transitions under applied magnetic fields. While the magnetic structure has not been previously reported, we leave detailed discussion of physics for a separate paper and focus here on testing the model-free framework for identifying magnetic phase transitions from this dataset.

The second dataset comprises temperature-dependent x-ray diffraction from $Cd_2Re_2O_7$, which exhibits a series of intriguing structural transitions still under active debate [29–33]. We use the same data previously analyzed with a physics-based ML study and again focus here on testing our entropy analysis on this representative total scattering dataset containing thousands of Bragg peaks and short-range diffuse scattering, in contrast with our first example of neutron diffraction dataset that contained a single Bragg peak. Details regarding the measurements are given in Ref. [18].

In the third case, we extend beyond the scattering data and show the robustness of our framework on real-space L-TEM images of Fe_3GeTe_2. Previous L-TEM results reveal thermally hysteretic behavior in Fe_3GeTe_2, dependent on the strength of the out-of-plane magnetic field [19]. A 2D phase transition associated with the Néel skyrmion lattice occurs in the 150–200 K temperature range for both field-cooled and field-heating protocols. Here, we focus on the same published dataset collected during field heating that exhibits a relatively sharp change in skyrmion order under an applied field of 500 G. In the L-TEM experiment, skyrmion lattice order, quantified by the local orientational order parameter, indicates a phase transition near 200 K [19]. Details regarding the measurements are given in Ref. [19].

IV. DEMONSTRATION OF ENTROPY ANALYSIS IN EXPERIMENTAL DATASETS

A. Temperature-dependent neutron diffraction in $Eu_3Sn_2S_7$

Figure 2(a) shows a raw detector image with a distinct magnetic Bragg peak at $\boldsymbol{Q} = (-0.5, 1.5, 0)$ r.l.u. at $T = 1.7$ K. The peak intensity decreases with increasing temperature and is absent at $T = 10$ K. The strong, localized intensity against near-zero background visually indicates a magnetically ordered state at low temperature. As shown in Fig. 2(b), the peak intensity vanishes above ∼6 K, consistent with an antiferromagnetic transition near this temperature. The Shannon entropy computed from these images is rather ambiguous, although it appears to saturate above 6 K [Fig. 2(b)]. This coincidence suggests that the Shannon entropy computed from raw data images captures the evolution of magnetic order in this material, with lower entropy corresponding to more ordered states.

Figure 2(c) displays the computed pairwise KLD matrix, which exhibits a square block below 6 K corresponding to the magnetically ordered phase. The low divergence values within this block reflect the statistical similarity among low-temperature states, distinct from high-temperature disordered phase. Similar blocklike structures also appear in the symmetric JD and JSD matrices, as well as in the Δ-KLD matrix [Figs. 2(d)–2(f)]. Notably, an additional transition is marginally visible near 4 K in Fig. 2(e). This feature is supported by magnetic susceptibility measurements and neutron diffraction at another wave vector, although it is not directly visible in temperature-dependent peak intensity in Fig. 2(b). Overall, these results suggest that our statistical analysis of raw neutron scattering data can identify potential phase transitions without requiring prior knowledge of the ordering wave vector or explicit model.

B. Field-induced transition in $Eu_3Sn_2S_7$

Since the analysis above does not explicitly require temperature as input, we can extend this approach to detect magnetic-field-dependent phase transitions. Figure 3(a) shows the field dependence ($\mu_0 H$) of the magnetic peak intensity at $\boldsymbol{Q} = (-0.5, 1.5, 0)$. Three prominent features are observed:

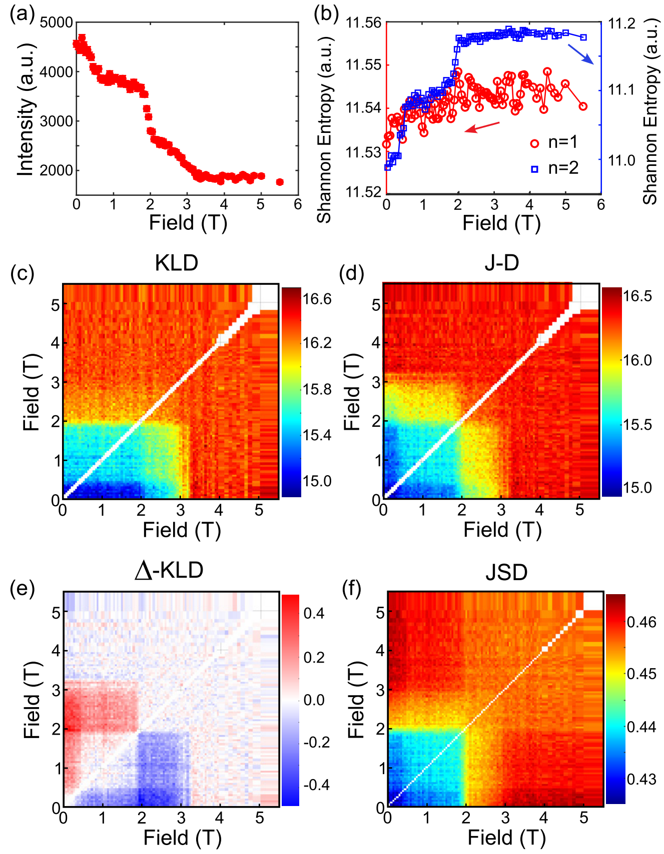

FIG. 3. (a) Magnetic field dependence of the magnetic Bragg peak intensity at $Q = (-0.5, 1.5, 0)$. (b) Shannon entropy ($n = 1$) and escort-weighted entropy ($n = 2$) as functions of magnetic field. (c)–(f) Divergence matrices highlighting a series of field-induced transitions at 0.5, 2, and 3 T.

Two sharp intensity drops signaling field-induced metamagnetic transitions at $\mu_0 H = 0.5$ and 2 T, and a change in slope above 3 T consistent with magnetization saturation. Figure 3(b) shows the Shannon entropy as a function of field; however, it is noisy, not providing a clear indication of phase transitions. In contrast, the escort-weighted entropy with exponent $n = 2$, plotted in the same figure, effectively reduces the weight of background (discussed in Sec. V) and clearly reveals the two field-induced transitions around 0.5 and 2 T. Figures 3(c)–3(f) display the four divergence matrices computed based on the escort distribution ($n = 2$). Their color maps exhibit similar blocklike structures whose boundaries align with the transitions identified from the peak intensity in Fig. 3(a). As we have shown, introducing the escort distribution into the calculation of entropy and divergences significantly enhances the sensitivity and robustness of entropy analysis for detecting subtle phase transitions.

C. Detecting diffuse scattering and multiple transitions in $Cd_2Re_2O_7$

Owing to the brightness of synchrotron sources and the development of pixelated detectors, it is now efficient to collect large (several terabytes) datasets of single crystal x-ray scattering. To examine the applicability of the entropy

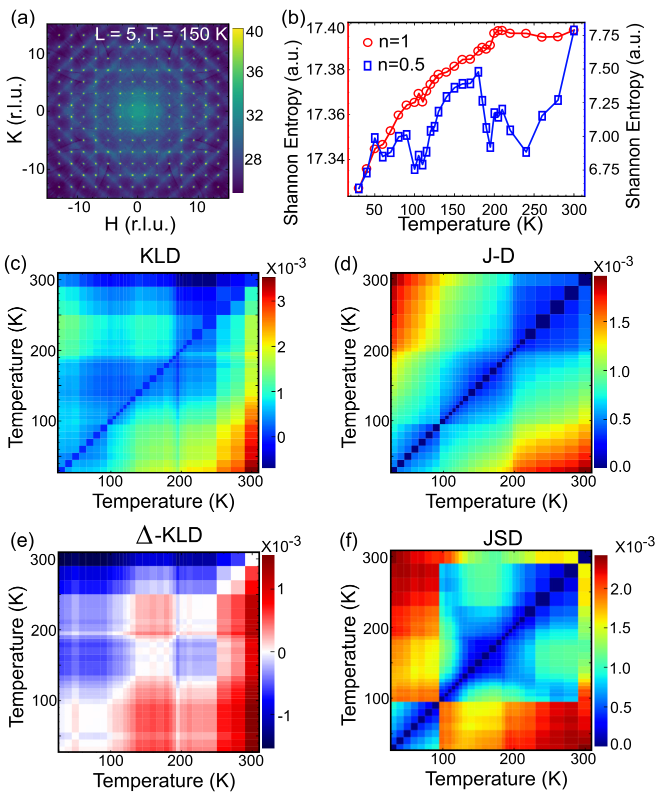

FIG. 4. (a) A [H, K, 0] slice of the x-ray scattering data for $Cd_2Re_2O_7$ measured at 150 K. (b) Shannon entropy ($n = 1$) and escort-weighted entropy ($n = 0.5$) as functions of temperature. (c)–(f) Divergence matrices revealing transitions near 100, 130, 200, and 250 K.

analysis to such datasets, we applied it to our existing x-ray diffuse scattering data on $Cd_2Re_2O_7$, which exhibits intriguing phase transitions and diffuse scattering. Figure 4(a) presents a slice of scattering data in Q space at 150 K, with both Bragg peaks and diffuse scattering clearly visible. Figure 4(b) shows the computed Shannon entropy ($n = 1$) and the escort-weighted entropy ($n = 0.5$). While the two curves exhibit completely different behaviors, they both show features across the phase transitions near 200 and 100 K. We further computed all four divergence matrices using different values of n ranging from 0.125 to 1, shown in Figs. 4(c)–4(f).

Previous studies have shown that $Cd_2Re_2O_7$ undergoes a second-order phase transition at $T_{s1} = 200$ K from the high-temperature cubic pyrochlore $Fd\bar{3}m$ structure to an intermediate phase. This intermediate phase breaks inversion symmetry with the $I\bar{4}m2$ space group, corresponding to one component of the E_u order parameter [29], followed by a first-order transition at $T_{s2} = 113$ K to the $I4_122$ space group, the other component of E_u symmetry. Raman data further postulate a possible third transition at 80 K involving symmetry lowering into an orthorhombic structure [29]. A machine-learning-based analysis of the total x-ray scattering data, which clustered points in reconstructed reciprocal space by their temperature dependence, identified several temperature regions with different behavior [18]. Upon cooling from about 250 K, a buildup of order-parameter-like diffuse scattering was observed around two sets of Bragg peak positions as the system approached the second-order phase transition at T_{s1} (Fig. 2(a) in Ref. [18]). Below T_{s1}, new Bragg peaks of the $I\bar{4}m2$ structure emerged at the positions of these two sets, with one set having a larger amplitude than the other, though both increased with the same critical exponent. At T_{s2}, the intensities of these sets abruptly swapped amplitudes and then continued to increase at the same rate without any other changes in the long-range ordered structure. Strong diffuse scattering around these sets persisted throughout the range between T_{s1} and T_{s2}, but with the intensity around one set being much stronger than around the other. Both diffuse scattering contributions initially decreased below T_{s1} but were found to increase again below about 130 K toward T_{s2}, and then decreased with different behavior below T_{s2}, where they also swapped the ratio of their intensities (see Fig. 4(c) of Ref. [18]). No signature of another transition at 80 K was observed.

These observations were interpreted as the buildup of diffuse scattering due to a soft phonon leading to the phase transition at T_{s1}, which splits into a Higgs mode and a Goldstone mode below T_{s1}. The Goldstone mode arises from fluctuations between the two components ($I\bar{4}m2$ and $I4_122$) of the E_u order parameter. Its energy rises slightly below T_{s1}, leading to a decrease of the diffuse scattering. The Goldstone mode energy then approaches zero again as fluctuations shift from the $I\bar{4}m2$ to the $I4_122$ symmetry near T_{s2}, causing the diffuse scattering to increase. Below T_{s2}, the Goldstone mode energy increases again, and the behavior of the diffuse scattering in the two sets changes relative to that above T_{s2}, as explained by a swap of the sign of sixth- and eighth-order terms in a Landau expansion (see Fig. 4 and related discussion in Ref. [18]). This analysis, while providing detailed physical insights, required two separate ML runs on the temperature-dependent x-ray data, with one for the strong Bragg peaks and another for the much weaker diffuse scattering, with a fixed number of distinct phases and detailed theoretical interpretation of the results.

Our divergence matrices clearly reveal these different regions with distinct behavior without any prior physics knowledge. The Δ-KLD, shown in Fig. 4(e), reveals five blocks along the diagonal direction, separated by four transitions at 90, 130, 200, and 250 K. The transitions at 90 and 200 K are also clearly visible in the JD, while the JSD matrix shows a sharp transition at 90 K, a broader one at 130 K, and a broad transition near 200 K. By comparison with the detailed previous physical analysis in Ref. [18], it becomes clear that the block in Δ-KLD from 250 to 300 K corresponds to the region in the cubic structure without appreciable fluctuations of the lower-temperature tetragonal phase. The second block, from 250 K to T_{s1}, marks the onset of diffuse scattering due to the soft-mode transition, with a sharp boundary at T_{s1} signaling the onset of a long-range ordered $I\bar{4}m2$ phase. The next transition, observed in both the Δ-KLD and the KLD, reflects the crossover from diffuse scattering dominated by critical fluctuations to that dominated by Goldstone mode fluctuations. Finally, the transition at 90 K marks the disappearance of the diffuse scattering into the background, possibly associated with a further lowering of symmetry observed in Raman studies. While both the JD and JSD clearly show transitions between regions with markedly different behavior of the data, e.g., onset of long-range-order Bragg peaks and the disappearance of diffuse scattering, they are less sensitive to the more subtle change in the character of the diffuse scattering at 130 K. It is interesting to note that none of the divergence matrices marks the transition at T_{s2} itself; instead, they indicate the changes in diffuse scattering associated with this transition. In contrast, the T_{s1} transition is clearly observed in all matrices, as are all other transitions in the other datasets analyzed. We attribute this to the rather special behavior of the $I\bar{4}m2$ to $I4_122$ transition, where the two sets of Bragg peaks distinct from the cubic structure swap intensities, resulting in no net change in entropy. This interpretation is further in agreement with the physical interpretation of this being a transition between two components of the E_u mode.

While our entropy analysis cannot provide a physical interpretation for the different temperature regimes observed, the entropies and divergence matrices can be calculated instantly from raw data. Moreover, the differences among Δ-KLD, JD, and JSD can provide indications of the origin of different transitions. More subtle transitions, possibly due to short-range order and fluctuations, are most visible in the KLD and Δ-KLD, whereas long-range order are more apparent in the entropy, JD and JSD. The instantaneous indication of the onset of a transition can be used to guide experiments on the fly, and the determination of the number of different regions provides important input for further physics-based analysis. These results clearly demonstrate the advantage of our entropy analysis approach in identifying complex phase transitions in large datasets without requiring prior structural models.

D. Detection of phase change/transition of magnetic skyrmions in Fe_3GeTe_2

In the previous scattering experiments, the intensity at each pixel or voxel can be directly related to a specific $\boldsymbol{Q}$-state of the system via Fourier transformation. However, this connection is not as straightforward when processing real-space imaging datasets. In the following case, we demonstrate that the same entropy analysis technique can be applied to a broad range of data types beyond reciprocal-space measurements. Here, we use our previously published L-TEM datasets of Fe_3GeTe_2, which was found to host a transition in its two-dimensional magnetic skyrmion lattice [19]. Figure 5(a) displays a representative L-TEM image of a Néel skyrmion lattice at 100 K. Previous statistical analysis, with machine-learning-assisted image processing, indicated a transition from a disordered skyrmion lattice to a more ordered phase as the temperature approaches 200 K [19]. Figure 5(b) presents both the Shannon ($n = 1$) and escort-weighted ($n = 2$) entropies, showing similar increases upon field heating. These entropy changes coincide with the emergence of orientational partial ordering of magnetic skyrmions. Figures 5(c)–5(f) show the computed divergence matrices based on the escort distribution ($n = 2$). The color maps reveal a clear square block below ∼180 K, with a crossover between 180 and 210 K. The boundary between low-temperature and high-temperature states, however, is less sharp than those observed in Figs. 2–4, likely due to the intrinsic 2D nature of the transition. Our published work suggests that this transition is associated with both long-range translational effects and

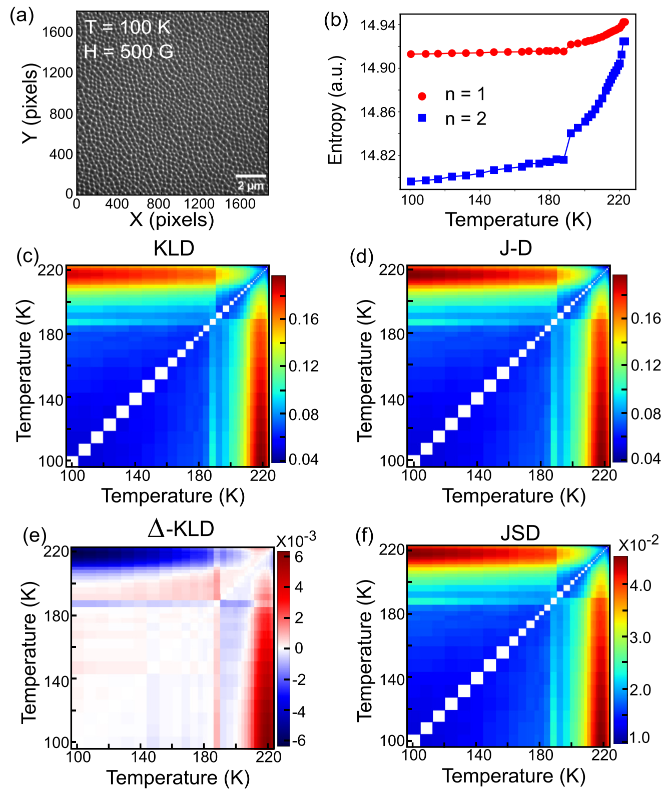

FIG. 5. (a) Lorentz-TEM image of magnetic skyrmions in Fe_3GeTe_2 at $T = 100$ K. (b) Shannon entropy ($n = 1$) and escort-weighted entropy ($n = 2$) as functions of temperature. (c)–(f) Divergence matrices highlighting the restoration of orientational order in the skyrmion lattice around 200 K.

local orientational order. While our entropy analysis does not directly probe the local orientational order parameter, our results in Fig. 5 might reflect the statistical variation associated with skyrmion sizes and/or densities. Nevertheless, the close correspondence between the material's phase evolution and the divergence matrices in Figs. 5(c)–5(f) demonstrates that our entropy analysis framework robustly applies to real-space imaging datasets.

V. DISCUSSION

Having demonstrated the practical advantages of this entropy analysis framework, we now discuss its implications. In principle, experimental observation can be considered as an information transfer process, wherein the vast degrees of freedom in a physical system are reduced to finite datasets via an unknown transformation (Fig. 1) depending on the experimental methods and parameters, such as instrument geometry, coherence loss, limited elemental contrast, finite detector coverage, etc. Therefore, only a fraction of the total information can be captured in a single experiment, which may not suffice to uniquely determine the ground truth. In fact, comparing measured observables from complementary experimental approaches is necessary and frequently used in discovering hidden phases in the past. For instance, in water ice [34,35], it is well known that thermodynamic measurements fail to capture the partially frozen degrees of freedom according to the so-called "ice rule," resulting in the discovery of residual entropy when compared to spectroscopic measurements. A similar practice was also conducted by A. Ramirez in the discovery of zero-point entropy in spin ice [2,36,37], defined as the difference between the measured entropy from specific heat data and that of an assumed high-temperature paramagnetic phase.

Although there exists considerable ambiguity in interpreting the computed entropy, some intuitive understanding can be obtained for typical scattering experiments, which is essentially a Fourier transformation of atomic positions or electron density distribution, with the weight of each pixel (voxel) corresponding to the probability of a specific $\boldsymbol{Q}$-state of the system. Due to the incomplete coverage of the reciprocal space, however, the measured probability distribution contains partial information, representing a conditional probability distribution [8] rather than the true distribution. Our introduction of the escort distribution essentially establishes an approximate connection between the conditional probability distribution and the ground truth. While such an approximation has not been rigorously proved, the framework is empirically supported by its consistent performance across all tested datasets, and its primary value lies in practical utility rather than mathematical rigor.

We can gain further insights into our entropy analysis through analogy with thermodynamic entropy. First, the divergence matrices quantify statistical changes in entropy between different macroscopic states separated by a small change of an external parameter (e.g., ΔT) and are therefore analogous to a specific heat measurement based on small temperature increments. By taking a line cut slightly off the diagonal of a divergence matrix, such as $D_{\mathrm{KL}}(T, T+\Delta T)$ from the KLD matrix, one can obtain a curve analogous to specific heat. Just as peaks in specific heat signal phase transitions in thermodynamic measurements, peaks or shoulders (manifested as a corner of the block structure in divergence matrices) in the off-diagonal curve signal statistical phase changes in data space.

Second, the introduction of the escort distribution with a tunable exponent n, or T_a, effectively controls the "temperature" of the measured datasets. For instance, an escort distribution with $n > 1$ (equivalently, $T_a < 1$) amplifies high-valued, more singular regions of the original distribution, analogous to cooling a system and concentrating population in low-energy states. Conversely, for $n < 1$, it enhances less-populated regions, resembling heating. To illustrate how T_a modulates the estimated entropy, we present a phase diagram [38] of the escort-weighted entropy with varied T_a in Fig. 6, using the field-dependent datasets of $Eu_3Sn_2S_7$. The corresponding phase diagrams for other datasets are provided in the Supplemental Material [38]. Because the calculated entropy can vary by several orders of magnitude, we visualize the results by normalizing the minimum and maximum of each field-dependent entropy curve (horizontal line in Fig. 6) to 0 and 1, respectively. The artificial temperature T_a is plotted on a logarithmic scale, with $\log_2 T_a = 0$ corresponding to the original Shannon entropy.

In Fig. 6, we find that the escort-weighted entropy is noisy at high artificial temperatures, though some visible transitions appear near the field of ~2 T. As T_a is reduced, the computed

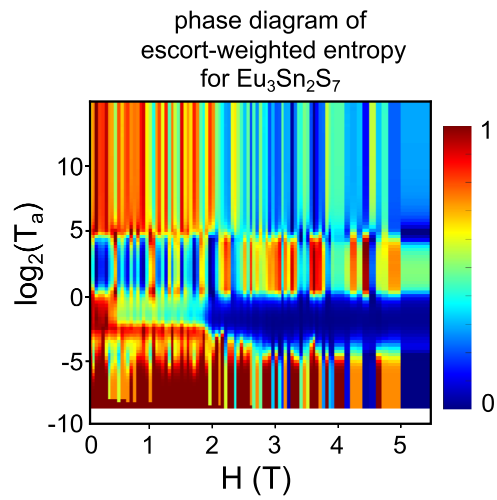

FIG. 6. Diagram of escort-weighted entropy as a function of T_a from the field-dependent $Eu_3Sn_2S_7$ dataset. The horizontal axis denotes magnetic field, and the vertical axis is the artificial temperature T_a, shown on a logarithmic scale. Each row is normalized between its minimum and maximum to emphasize the relative variation within that row.

escort-weighted entropy enters a critical region in which its field dependence exhibits well-structured features with a visibly high signal-to-noise ratio. As T_a decreases further, this region terminates at a lower bound, beyond which the entropy curve becomes noisy again. In the limit $T_a \to 0$, the escort distribution is expected to condense toward a "ground state" dominated by one or a few pixels/voxels, while the rest carry zero weight. Within the critical region of T_a, we found that the divergence matrices consistently produce blocklike features, confirming that well-defined phase boundaries persist in this regime. Interestingly, across all the datasets we have tested (Figs. 2–5), the optimal value of T_a falls in the region with $\log_2 T_a$ close to 0. This empirical finding suggests that, for the experimental configurations studied here, the measurement process approximately preserves the statistical structure of the physical state distribution, providing a nontrivial validation of the postulated mapping in Eq. (1). Therefore, the value of T_a might also be useful as a rough indicator of the "efficiency" of a proposed measurement.

In practice, we recommend computing the phase diagram of escort-weighted entropy as a function of $\log_2 T_a$ with a finite range (as shown in Fig. 6 and in the Supplemental Material [38] for all datasets) to determine a suitable value of n or T_a. This diagram provides a systematic way to identify the region of artificial temperature in which phase boundaries are clearly resolved. Since the nature of the raw probability distribution is largely affected by the experimental setup, the optimal value of n is unlikely to vary significantly once the instrumental configuration is fixed. This opens the possibility of calibrating n once for a given instrument and measurement type and reusing it across similar measurements without recomputing the full phase diagram each time.

Beyond the selection of T_a, we envision this entropy-based analysis as a fast screening tool rather than a replacement for conventional model-based analysis. Its primary added value lies in three aspects: (1) it provides a bias-free, model-independent screening of experimental data, reducing the risk of overlooking unexpected phase transitions that may occur at unanticipated wave vectors or involve subtle redistribution of spectral weight; (2) it offers rapid, automated detection of the onset of candidate phase transitions, which is particularly valuable during ongoing experiments when beamtime is limited and rapid decisions are required [38]; and (3) the results can serve as input for more advanced analysis pipelines, for example, by providing initial estimates of the number of phases or transition temperatures as hyperparameters for machine-learning workflows [17,18].

VI. CONCLUSION

In conclusion, we have developed an entropy-based analysis framework that connects the thermodynamic entropy of materials and the informational entropy in experimental datasets. By transforming measured data into an escort distribution, we can associate changes in Shannon entropy of the datasets with the formation of various physical orders in materials, including long- and short-range magnetic and structural orders as well as nontrivial orientational order in topological spin textures. We introduced four divergence matrices (KLD, JD, JSD, and Δ-KLD) that collectively provide comprehensive measures of potential phase transitions without explicit models or prior knowledge and in contrast to traditional methods, e.g., of measuring the temperature dependence of a single or few particular peaks, avoids misidentification or not observing transitions due to selection bias. This method provides very quickly basic information regarding changes in the character of large datasets to guide more detailed physical analysis. We demonstrated that this framework is broadly applicable to diverse datasets and experimental probes, including neutron/x-ray scattering and real-space imaging.

As data collection rates in modern experiments continue to increase with technical advances such as large-area detectors and higher flux sources, model-free, real-time informatics provides important and efficient guidance during experimentation and complements traditional model-dependent analysis. Immediate extension includes application to time-resolved x-ray photon correlation spectroscopy measurements, which can provide richer statistical signatures. Further developments such as on-the-fly entropy analysis operating directly in raw data space and integration into advanced machine-learning workflows may yield insights into increasingly complex experimental datasets.

ACKNOWLEDGMENTS

Y.L. and S.R. thank Jacob Ruff for insightful discussions regarding image compression and entropy estimation. This work was supported by the U.S. Department of Energy, Office of Science, Basic Energy Sciences, Materials Sciences and Engineering Division. Y.C. and B.T.F. further thank the U.S. Department of Energy, Office of Science for the Early Career Research Program for simulating the atomic disorder in ideal systems. This research used resources at the Advanced Photon Source, a U.S. DOE Office of Science User Facility operated by Argonne National Laboratory. A portion of this research used resources at the High Flux Isotope Reactor, a DOE Office of Science User Facility operated by the Oak Ridge National Laboratory. The beam time was allocated to HB-3A on Proposals No. IPTS-32168 and No. IPTS-33344. Use of the Center for Nanoscale Materials, an Office of Science user facility, was supported by the U.S. Department of Energy, Office of Science, Office of Basic Energy Sciences, under Contract No. DE-AC02-06CH11357.

DATA AVAILABILITY

Data of $Cd_2Re_2O_7$ have been made publicly available in previous publication (see Ref. [18]). The data of $Eu_3Sn_2S_7$ and Fe_3GeTe_2 are available from the authors upon reasonable request.

[1] J. Villain, R. Bidaux, J. P. Carton, and R. Conte, Order as an effect of disorder, J. Phys. **41**, 1263 (1980).

[2] A. P. Ramirez, A. Hayashi, R. J. Cava, R. Siddharthan, and B. S. Shastry, Zero-point entropy in 'spin ice', Nature (London) **399**, 333 (1999).

[3] S. W. Hawking, Particle creation by black holes, Commun Math. Phys. **43**, 199 (1975).

[4] E. Verlinde, On the origin of gravity and the laws of Newton, J. High Energy Phys. 04 (2011) 029.

[5] C. E. Shannon, A mathematical theory of communication, Bell Syst. Tech. J. **27**, 379 (1948).

[6] C. E. Shannon, A mathematical theory of communication, Bell Syst. Tech. J. **27**, 623 (1948).

[7] E. T. Jaynes, Information theory and statistical mechanics, Phys. Rev. **106**, 620 (1957).

[8] E. T. Jaynes, Part I principles and elementary applications, in *Probability Theory the logic of Science*, edited by G. L. Bretthorst (Cambridge University Press, Cambridge, 2003), pp. 1–339.

[9] R. Landauer, Irreversibility and heat generation in the computing process, IBM J. Res. Dev. **5**, 183 (1961).

[10] J. Hong, B. Lambson, S. Dhuey, and J. Bokor, Experimental test of Landauer's principle in single-bit operations on nanomagnetic memory bits, Sci. Adv. **2**, e1501492 (2016).

[11] A. Bérut, A. Arakelyan, A. Petrosyan, S. Ciliberto, R. Dillenschneider, and E. Lutz, Experimental verification of Landauer's principle linking information and thermodynamics, Nature (London) **483**, 187 (2012).

[12] A. Scheie, P. Laurell, A. M. Samarakoon, B. Lake, S. E. Nagler, G. E. Granroth, S. Okamoto, G. Alvarez, and D. A. Tennant, Witnessing entanglement in quantum magnets using neutron scattering, Phys. Rev. B **103**, 224434 (2021).

[13] M. J. Krogstad, P. M. Gehring, S. Rosenkranz, R. Osborn, F. Ye, Y. Liu, J. P. C. Ruff, W. Chen, J. M. Wozniak, H. Luo, O. Chmaissem, Z.-G. Ye, and D. Phelan, The relation of local order to material properties in relaxor ferroelectrics, Nat. Mater. **17**, 718 (2018).

[14] Y. Li, J. Coles, X. Gui, H. Park, Y. Wu, X. Chen, J.-H. Chen, X. Wang, H. Cao, S. Stadler, O. Chmaissem, D. Young, S. Rosenkranz, and J. Ditusa, Structural and magnetic properties of $CoTeMoO_6$, Phys. Rev. B **111**, 104434 (2025).
[15] Y. Li, Z. Liu, Z. Xu, Y. Song, Y. Huang, D. Shen, N. Ma, A. Li, S. Chi, M. Frontzek, H. Cao, Q. Huang, W. Wang, Y. Xie, R. Zhang, Y. Rong, W. A. Shelton, D. P. Young, J. F. DiTusa, and P. Dai, Flat-band magnetism and helical magnetic order in Ni-doped $SrCo_2As_2$, Phys. Rev. B **100**, 094446 (2019).
[16] T. R. Welberry and R. Whitfield, Single crystal diffuse neutron scattering, Quantum Beam Sci. **2**, 2 (2018).
[17] K. Mallayya, J. Straquadine, M. J. Krogstad, M. D. Bachmann, A. G. Singh, R. Osborn, S. Rosenkranz, I. R. Fisher, and E.-A. Kim, Bragg glass signatures in Pd_xErTe_3 with X-ray diffraction temperature clustering, Nat. Phys. **20**, 822 (2024).
[18] J. Venderley, K. Mallayya, M. Matty, M. Krogstad, J. Ruff, G. Pleiss, V. Kishore, D. Mandrus, D. Phelan, L. Poudel, A. G. Wilson, K. Weinberger, P. Upreti, M. Norman, S. Rosenkranz, R. Osborn, and E.-A. Kim, Harnessing interpretable and unsupervised machine learning to address big data from modern X-ray diffraction, Proc. Natl. Acad. Sci. USA **119**, e2109665119 (2022).
[19] A. McCray, Y. Li, R. Basnet, K. Pandey, J. Hu, D. Phelan, X. Ma, A. K. Petford-Long, and C. Phatak, Thermal hysteresis and ordering behavior of magnetic skyrmion lattices, Nano Lett. **22**, 7804 (2022).
[20] J.-F. Bercher, On escort distributions, q-gaussians and Fisher information, AIP Conf. Proc. **1305**, 208 (2011).
[21] C. Beck and F. Schloegl, *Thermodynamics of Chaotic Systems* (Cambridge University Press, Cambridge, 1993).
[22] S. Kullback and R. A. Leibler, On information and sufficiency, Ann. Math. Stat. **22**, 79 (1951).
[23] H. Jeffreys, An invariant form for the prior probability in estimation problems, Proc. R. Soc. London Ser. A **186**, 453 (1946).
[24] J. Lin, Divergence measures based on the Shannon entropy, IEEE Trans. Inf. Theory **37**, 145 (1991).
[25] D. P. Kingma and M. Welling, Auto-encoding variational Bayes, arXiv:1312.6114.
[26] G. Hinton, O. Vinyals, and J. Dean, Distilling the knowledge in a neural network, arXiv:1503.02531.
[27] E. Ressouche, V. Simonet, B. Canals, M. Gospodinov, and V. Skumryev, Magnetic frustration in an iron-based cairo pentagonal lattice, Phys. Rev. Lett. **103**, 267204 (2009).
[28] D. Mihaylova, X. Chen, H. Zhao, D. Phelan, S. Rosenkranz, and Y. Li, Non-equilibrium dynamics in geometrically frustrated spin glass $Bi_2Fe_3GaO_9$ with a Cairo lattice, J. Phys.: Condens. Matter **37**, 295802 (2025).
[29] Z. Hiroi, J.-I. Yamaura, T. C. Kobayashi, Y. Matsubayashi, and D. Hirai, Pyrochlore oxide superconductor $Cd_2Re_2O_7$ revisited, J. Phys. Soc. Jpn. **87**, 024702 (2018).
[30] K. J. Kapcia, M. Reedyk, M. Hajialamdari, A. Ptok, P. Piekarz, A. Schulz, F. S. Razavi, R. K. Kremer, and A. M. Oles, Discovery of a low-temperature orthorhombic phase of the $Cd_2Re_2O_7$ superconductor, Phys. Rev. Res. **2**, 033108 (2020).
[31] J. W. Harter, Z. Y. Zhao, J. Q. Yan, D. G. Mandrus, and D. Hsieh, A parity-breaking electronic nematic phase transition in the spin-orbit coupled metal $Cd_2Re_2O_7$, Science **356**, 295 (2017).
[32] M. R. Norman, Crystal structure of the inversion-breaking metal $Cd_2Re_2O_7$, Phys. Rev. B **101**, 045117(2020).
[33] S. Di Matteo and M. R. Norman, Nature of the tensor order in $Cd_2Re_2O_7$, Phys. Rev. B **96**, 115156 (2017).
[34] W. F. Giauque and M. F. Ashley, Molecular rotation in ice at 10°K. Free energy of formation and entropy of water, Phys. Rev. **43**, 81 (1933).
[35] W. F. Giauque and J. W. Stout, The entropy of water and the third law of thermodynamics. The heat capacity of ice from 15 to 273°K, J. Am. Chem. Soc. **58**, 1144 (1936).
[36] S. T. Bramwell and M. J. Harris, The history of spin ice, J. Phys.: Condens. Matter **32**, 374010 (2020).
[37] M. J. Harris, S. T. Bramwell, D. F. McMorrow, T. Zeiske, and K. W. Godfrey, Geometrical frustration in the ferromagnetic pyrochlore $Ho_2Ti_2O_7$, Phys. Rev. Lett. **79**, 2554 (1997).
[38] See Supplemental Material at http://link.aps.org/supplemental/10.1103/5txt-skp5 for a demonstration of on-the-fly analysis in raw data space and phase diagrams of other tested materials.